

1 **Interpretable Models Capture the Complex**
2 **Relationship Between Climate Indices and Fire Season**
3 **Intensity in Maritime Southeast Asia**

4 **William S. Daniels¹, Rebecca R. Buchholz², Helen M. Worden²,**
5 **Fatimah Ahamad³, Dorit M. Hammerling¹**

6 ¹Colorado School of Mines, Golden CO, USA

7 ²National Center for Atmospheric Research, Boulder CO, USA

8 ³AQ Expert Solutions, Jalan Dato Muda Linggi, Negeri Sembilan, Malaysia

9 **Key Points:**

- 10 • We quantify the connections between climate and carbon monoxide (as a proxy
11 for fire intensity) in more detail than previous work.
12 • Our model explains 70% of the variability in atmospheric carbon monoxide on a
13 weekly timescale using only climate mode indices.
14 • The impact of certain indices on carbon monoxide variability changes as their lead
15 time in the model increases.

Corresponding author: William Daniels, wdaniels@mines.edu

Abstract

There have been many extreme fire seasons in Maritime Southeast Asia (MSEA) over the last two decades, a trend which will likely continue or accelerate due to climate change. Fires, in turn, are a major driver of atmospheric carbon monoxide (CO) variability, especially in the Southern Hemisphere. Here we attempt to maximize the amount of CO variability that can be explained via human-interpretable statistical models that use only climate mode indices as predictor variables. We expand upon previous work through the complexity at which we study the connections between climate mode indices and atmospheric CO (a proxy for fire intensity). Specifically, we present three modeling advancements. First, we analyze five different climate modes at a weekly timescale, which increases explained variability by 15% over models on a monthly timescale. Second, we accommodate multiple lead times for each climate mode index, finding that some indices have very different effects on CO at different lead times. Finally, we model the interactions between climate mode indices at weekly timescales, which provides a framework for studying these interactions at a higher level of complexity than previous work. Furthermore, we perform a stability analysis and show that our model for the MSEA region is robust, which adds weight to the scientific interpretation of the selected model terms. We believe that the complex relationships quantified here will be useful for scientists studying modes of variability in MSEA and for forecasters looking to maximize the information they glean from climate modes.

1 Introduction

The relationship between fire and climate has been extensively studied. Fire intensity and burned area are related to the amount, type, and dryness of available fuel, all of which respond closely to water conditions driven by climate variability (van der Werf et al., 2008). This relationship is complex and varies across the different regions of the globe. For instance, drought conditions were found to increase fire potential in Southern Africa, but decrease fire potential in Northern Africa (Andela & van der Werf, 2014).

Climate modes, such as the El Niño Southern Oscillation (ENSO), capture variability in the global climate system. Studies have used these climate modes to help explain the complex relationship between climate and fire, often via regression models. ENSO has been found to influence fires in North America (Mason et al., 2017; Shabbar et al., 2011), Maritime Southeast Asia (Chen et al., 2017; Fuller & Murphy, 2006; Reid et al., 2012), the Amazon (Alencar et al., 2011; Fonseca et al., 2017), and Africa (Andela & van der Werf, 2014; N'Datchoh et al., 2015). Furthermore, studies have found that fire behavior can respond to several distinct climate modes (Andreoli & Kayano, 2006; Chen et al., 2016; Saji & Yamagata, 2003), with Cleverly et al. (2016) showing that the interactions between these climate modes are particularly important for explaining drought and rainfall in Australia (which in turn are major drivers of fire activity). This indicates that fire behavior is affected not only by the isolated influence of multiple modes, but also by their interactions (e.g., whether or not the modes are in phase).

In addition to identifying the climate modes that most influence fire behavior in a given region, studies such as Chen et al. (2016) and Wooster et al. (2012) identify lead times that correspond to the maximum predictive performance of the climate modes being studied. Similarly, Shawki et al. (2017) examines how far in advance the 2015 fire event in Indonesia can be predicted using climate based models, finding that lead times of up to 25 weeks can still provide useful predictions.

These fire-climate connections have been previously studied using satellite observations of fire properties (e.g., Ceccato et al. (2010), Chen et al. (2016), and Wooster et al. (2012)). The Moderate Resolution Imaging Spectroradiometer (MODIS) instruments onboard the Terra and Aqua satellites provide fire count data for each overpass as well

66 as a burned area data product (Giglio et al., 2006, 2016, 2018). However, using fire counts
67 or burned area directly presents a number of challenges. Fire count products ignore dif-
68 ferences in fire size and intensity, burned area products can miss underground peat fires,
69 and both products can miss fires obscured by smoke (Giglio et al., 2006, 2018; Shawki
70 et al., 2017).

71 One alternative is to model atmospheric carbon monoxide (CO) instead of fire counts,
72 burned area, or aerosol optical depth (AOD) directly. CO is produced by incomplete com-
73 bustion from biomass burning, fossil fuel use, and indirectly by photochemistry (Buchholz
74 et al., 2018; Holloway et al., 2000), and its link to fires is well established (Edwards, Em-
75 mons, et al., 2006). In fact, biomass burning is the primary source of atmospheric CO
76 variability in the Southern Hemisphere, making CO anomalies a useful proxy for fire in-
77 tensity (Bloom et al., 2015; Buchholz, Worden, Park, et al., 2021; Voulgarakis et al., 2015).
78 Buchholz, Worden, Park, et al. (2021) show that MODIS AOD and CO observations from
79 the Measurement of Pollution in the Troposphere (MOPITT) instrument over the Mar-
80 itime Southeast Asia (MSEA) region are highly correlated, further justifying the use of
81 CO as an alternative to fire products or AOD. Since CO variability in the Southern Hemi-
82 sphere is closely linked to biomass burning (and biomass burning responds to variabil-
83 ity in the climate), we expect that CO also responds to climate variability. Compared
84 to the study of fire counts, burned area, or AOD, less research has gone into the connec-
85 tion between atmospheric CO and climate variability. Furthermore, modeling atmospheric
86 CO concentrations provides information on co-emitted atmospheric pollutants in addi-
87 tion to being a proxy for fire intensity.

88 Edwards, Pétron, et al. (2006) found that CO observations from MOPITT are cor-
89 related with ENSO. Buchholz et al. (2018) expanded on Edwards, Pétron, et al. (2006)
90 by showing that atmospheric CO anomalies in a number of Southern Hemisphere regions
91 are related to four different climate modes (including ENSO) and that the interactions
92 between these climate modes are important for explaining atmospheric CO anomalies.
93 In this study, we examine the relationship between atmospheric CO and climate vari-
94 ability, further focusing on the MSEA region because of its extremely large CO anoma-
95 lies (Buchholz, Worden, Park, et al., 2021). While we focus on a single region in this pa-
96 per, the modeling framework we have developed can easily be applied to other parts of
97 the globe.

98 In this paper, we propose a framework for studying the connections between cli-
99 mate and atmospheric CO (as a proxy for fire intensity) in more detail than previous work.
100 To do this, we extend the models from Buchholz et al. (2018) via the following advance-
101 ments. First, we use week-averaged data rather than month-averaged data, significantly
102 increasing predictive performance. Second, we include the Madden-Julian Oscillation (MJO)
103 via a proxy index, resulting in models that are better able to capture extreme CO anoma-
104 lies in MSEA. Third, we develop a regularization-based model fitting framework that al-
105 lows for models with multiple lags of a single climate mode. Fourth, we assess the sta-
106 bility of the selected model terms, which adds weight to their scientific interpretation and
107 increases overall model interpretability. Finally, we explore the use of our model in a fore-
108 casting setting to assess how much variability can be explained using climate mode in-
109 dices alone. Note that we do not attempt to outperform or even match current forecast-
110 ing tools that utilize additional modes of variability beyond climate modes (e.g., Groot
111 et al. (2006), Shawki et al. (2017)), as we are only interested in the connections between
112 climate modes and CO. These advancements result in models that capture more com-
113 plex relationships and have better predictive performance than those presented in Buchholz
114 et al. (2018) while remaining human-interpretable. We believe that these models will be
115 useful for scientists studying modes of variability in MSEA and forecasters looking to
116 maximize the information they glean from climate modes.

117 The rest of this paper is laid out as follows. In Sections 2 and 3, we describe the
118 data and our statistical model, respectively. In Section 4, we discuss our model fitting

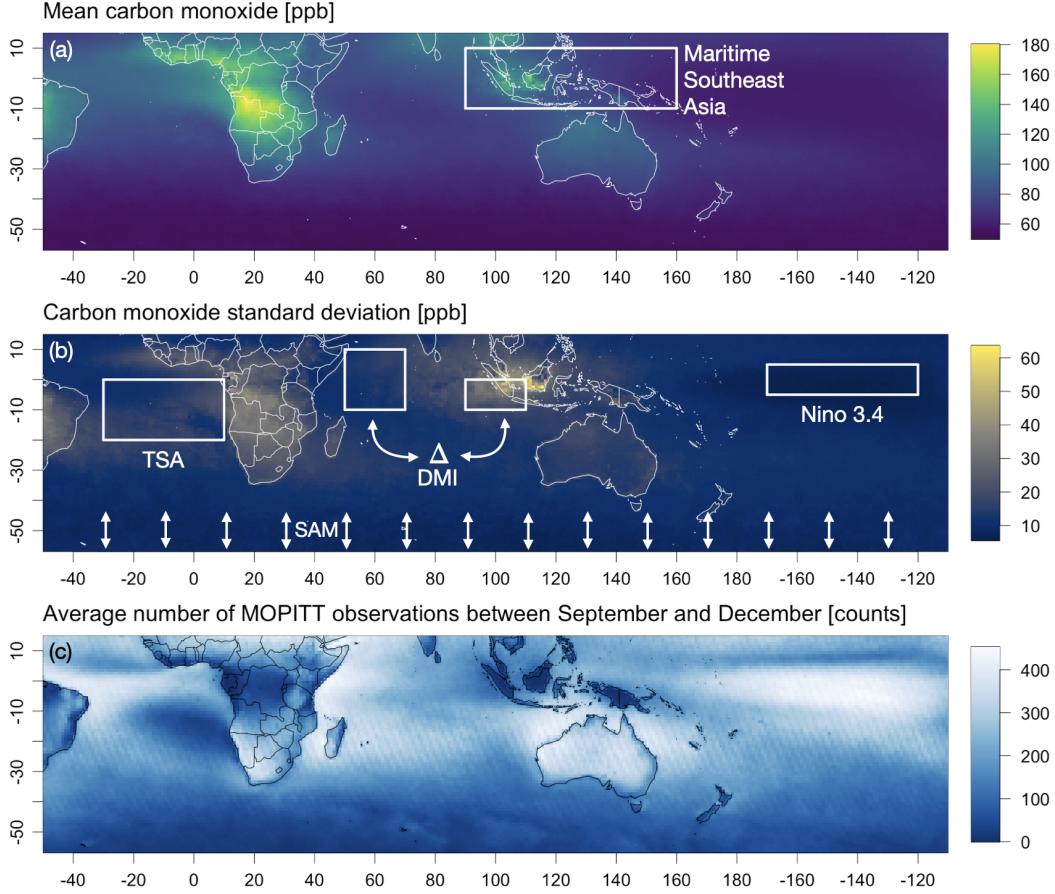


Figure 1. MOPITT CO data during the Southern Hemisphere fire season (defined here as September through December) from 2001 to 2019. Data are filtered as described in Section 2.1. (a) Average of all MOPITT CO observations ($n = 217,995,648$) with the Maritime Southeast Asia (MSEA) region shown in white ($n = 12,985,456$). (b) CO standard deviation with the spatial range of influence of the four climate mode indices discussed in Section 2.2 shown in white. (c) Average number of MOPITT observations falling within each grid cell during fire season. Note that the landmasses in MSEA have fewer observations than other regions, which could be influencing the high CO standard deviations in this region. All three subfigures are plotted on the same $1^\circ \times 1^\circ$ grid.

119 framework. In Sections 5 and 6, we present results and assess improvements in model
 120 interpretability and predictive performance, respectively, over the models presented in
 121 Buchholz et al. (2018). Finally, we summarize our work in Section 7.

122 2 Observational Data Sets

123 We model atmospheric CO using a linear regression framework in which the response
 124 variable (CO) is modeled as a linear combination of predictor variables (climate mode
 125 indices and their proxies). The following subsections describe the data used as our re-
 126 sponse and predictor variables. Note that “covariate” is synonymous with “predictor vari-
 127 able” and is used throughout for brevity.

128

2.1 Response Variable

129

130

131

132

133

134

For the response, we use carbon monoxide column-averaged volume mixing ratios (referred to as simply CO) from the MOPITT instrument onboard the Terra satellite (Drummond et al., 2010). The units of column-averaged volume mixing ratios (VMR) are parts per billion by volume (ppb). Using column-averaged volume mixing ratios instead of total column CO removes dependence on surface topography and pressure changes (Buchholz, Worden, Park, et al., 2021).

135

136

137

138

139

140

141

142

MOPITT has complete Earth coverage about every three days with a footprint size of $22 \times 22 \text{ km}^2$. We use the V8 retrieval algorithm with validation results described in Deeter et al. (2019). To reduce systematic and random error, we select daytime, land-only retrievals from the joint near infrared (NIR) and thermal infrared (TIR) product. Daytime retrievals over land have a higher sensitivity to CO than nighttime or ocean retrievals due to higher thermal contrast. We use the joint product because it includes additional information from reflected solar radiation over land (Worden et al., 2010). See Buchholz et al. (2018), Deeter et al. (2007), and Deeter et al. (2014) for details.

143

144

145

146

147

148

149

150

151

152

153

154

155

Because MOPITT retrievals are dependent on clear sky conditions, we expect sampling error to both bias our CO time series lower and increase its variability. This is because MOPITT observations might not be available nearest to fire source regions and cloud patterns can significantly reduce the amount of data available over the region. This issue is also present in other satellite-observed data sets, such as fire counts or aerosol optical depth (Reid et al., 2012). However, we do not expect these features to significantly impact our results for two reasons. First, the magnitude of the response will only impact the magnitude of the fitted coefficients, not their relationship relative to each other. Therefore, interpretation of selected model terms is still valid in a relative sense. Second, linear models fit via regularization (which we employ and discuss in Sections 3 and 4) are well suited for handling noisy or variable data and will not overfit to the noise when tuned correctly. An analysis of how much variability in our response is attributed to cloud sampling is the focus of another study.

156

157

158

159

160

161

162

163

164

165

166

167

168

169

170

171

172

173

We aggregate CO observations into a single biomass burning region in the Southern Hemisphere: Maritime Southeast Asia (MSEA), defined here as -10° to 10° latitude and 90° to 160° longitude (see Figure 1(a)). We focus on MSEA because it is a biomass burning region that experiences significant CO anomalies, or concentrations well above average (Buchholz, Worden, Park, et al., 2021). Note that there are fewer MOPITT observations over land within the MSEA region on average (see Figure 1(c)). This is likely a result of higher cloud fractions and geophysical noise over land scenes compared to water scenes in MSEA. The Supporting Information file contains a plot and discussion of the cloud fraction from the Terra-MODIS cloud mask over MSEA. We create a weekly time series for MSEA by averaging all of the observations falling within the region boundaries for each week. This time series ranges from 2001 to 2019, resulting in 19 years of data and 991 weekly averages. Despite the relatively lower number of observations falling over MSEA landmasses, there are still 110 observations per week on average, which we deem a suitable number for creating our response variable. We compute the seasonal cycle by taking an average over the 19 years of data for each week. We then remove this seasonal cycle from the weekly time series so that our models are better able to capture the anomalous CO observations corresponding to large burn events. Figure 2 shows the weekly CO observations, climatological average, and resulting anomalies for MSEA.

174

175

176

177

178

Finally, since we use CO as a proxy for fire intensity, we only model anomalies during the months that experience high CO variability due to burning. Although CO variability is highest between September and November in MSEA, we use anomalies between September and December to be consistent with Buchholz et al. (2018). This time frame results in a total of 330 weekly CO anomalies for the MSEA region.

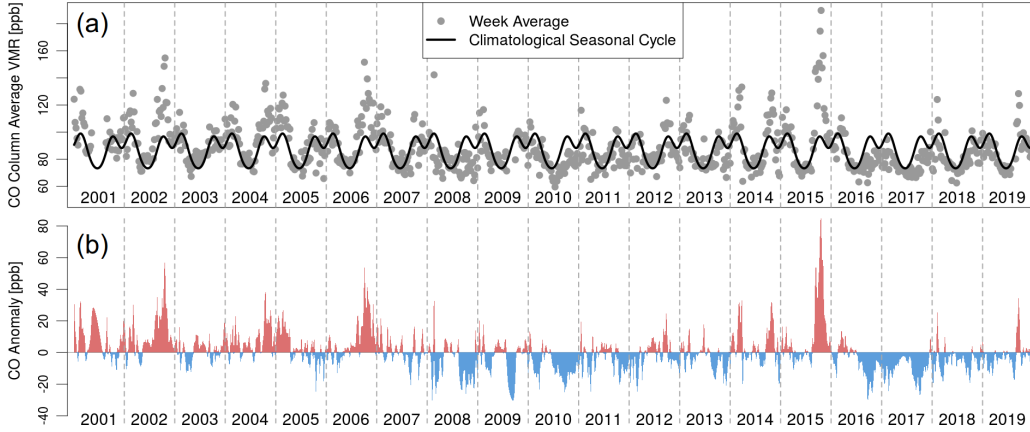


Figure 2. (a) Weekly CO observations for MSEA (grey circles) and the climatological average created by averaging each week over the 19-year time series (black line). (b) CO anomalies resulting from the difference between the weekly observations and the climatological average. Positive anomalies are shown in red and negative anomalies are shown in blue.

179

2.2 Predictor Variables

180

181

182

183

184

185

We are interested in connections between atmospheric CO and climate variability. Climate modes are large scale patterns that capture variation in temperature, wind, or other aspects of climate over certain spatial regions. A well known example is ENSO, which captures quasi-periodic variability in sea surface temperature and wind in the Pacific Ocean (Neelin et al., 1998; Trenberth, 2013). Climate indices are metrics that quantify the state of climate modes.

186

187

188

189

190

As in Buchholz et al. (2018), we consider four climate modes that represent variability in the major ocean basins of the Southern Hemisphere and tropics. The ENSO represents the Pacific Ocean, the Indian Ocean Dipole (IOD) represents the Indian Ocean, the Tropical South Atlantic (TSA) represents the southern Atlantic Ocean, and the Antarctic Oscillation (AAO) represents the Southern Ocean.

191

192

193

194

195

196

197

198

199

200

201

202

203

204

205

206

207

For predictor variables, we select a single climate mode index to represent each of these climate modes. To represent the ENSO, we use the Niño 3.4 index defined in Bamston et al. (1997). To represent the TSA, we use the Tropical South Atlantic Index defined in Enfield et al. (1999). These two indices are calculated using sea surface temperature (SST) anomalies in the regions shown in Figure 1(b) labeled as Niño 3.4 and TSA, respectively. To represent the IOD, we use the Dipole Mode Index (DMI) defined in Saji et al. (1999). This index is calculated from SST gradients between the two regions shown in Figure 1(b) labeled as DMI. To represent the AAO, we use the Southern Annular Mode (SAM) index defined in Thompson and Wallace (2000). This index captures Antarctic atmospheric circulation described by the poleward shift of westerly winds. This index is calculated by projecting observational height anomalies at 700 hPa and poleward of -20 degrees latitude onto the leading empirical orthogonal function of the National Centers for Environmental Prediction and National Center for Atmospheric Research reanalysis (Kalnay et al., 1996; Kistler et al., 2001). The spatial extent of this index is shown in Figure 1(b) via the arrows labeled SAM. We expect a relationship between these indices and CO, as each index is related to regional climate (e.g., rainfall), which in turn affects drought, fire, and ultimately CO concentrations.

208

209

In addition to these four indices, we also want to include variability captured by the MJO in our models. This climate mode broadly describes the eastward propagation

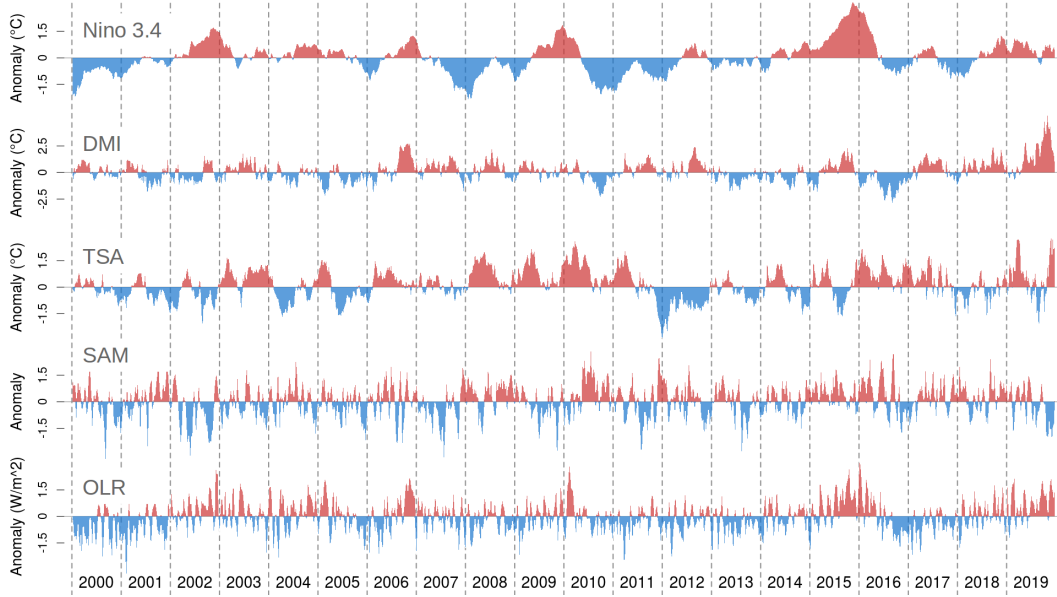


Figure 3. Time series of the five climate mode indices used as predictor variables in this study. Note that OLR is used as a proxy index for the MJO and that DMI is plotted using a different vertical scale.

210 of a convection cell that forms off the east coast of Africa and dissipates in the Pacific Ocean
 211 (Madden & Julian, 1972). The MJO is the dominant mode of intraseasonal variability
 212 in the tropics (Madden & Julian, 1994) and has been shown to increase or decrease the
 213 probability of extreme rain events by over 20% in MSEA depending on its phase (Xavier
 214 et al., 2014). The most common MJO index is described by the two primary empirical
 215 orthogonal functions (EOFs) resulting from a number of climate variables (Wheeler &
 216 Hendon, 2004). However, this index is poorly suited for use in a regression framework,
 217 as it would require a main term for both EOFs and their interaction to properly cap-
 218 ture the phase of the MJO. This introduces multiple coefficient estimates for a single phys-
 219 ical phenomenon, which makes it harder to model and hinders model interpretability.

220 Instead of using these EOFs, we use outgoing longwave radiation (OLR) anom-
 221 alies to approximate the variability described by the MJO. OLR is a metric that describes
 222 how much energy is leaving the atmosphere and is one climate variable used in Wheeler
 223 and Hendon (2004) to produce the EOF index. Low OLR values indicate the presence
 224 of clouds, and hence a higher likelihood of rainfall (Birch et al., 2016). While not per-
 225 fect, we believe OLR to be a decent approximation of the variability described by the
 226 MJO. Dias et al. (2017) shows that the MJO can be characterized by the variance in con-
 227 vection, and in Figure 3, we show that the frequency of the OLR signal captures the 30
 228 – 90 day oscillatory movement of the MJO convection cell. This OLR proxy is better suited
 229 for a regression analysis despite losing some of the information contained in the EOF in-
 230 dex from Wheeler and Hendon (2004).

231 We aggregate OLR values over the same spatial region that defines the MSEA re-
 232 gion shown in Figure 1, and we create anomalies in the same manner as the CO anom-
 233 alies described in Section 2.1. We demonstrate the benefit of including the OLR proxy
 234 in Section 6.1.

235 Figure 3 shows the weekly time series for each climate mode index used as a pre-
 236 dictor variable in this study. Some of the indices have both high and low frequency com-

237 ponents. This is most obvious in the SAM and OLR. We believe that the high frequency
 238 component of the OLR captures the oscillatory movement of the convection cell described
 239 by the MJO because both have a period of around 30 to 90 days. The climate mode in-
 240 dex data used in this study are publicly available. The source of each index (or proxy
 241 index in the case of the MJO) is listed in Table 1.

Table 1. Climate mode indices used in this study with citations for their sources. Note that we use OLR as a proxy index for the MJO.

Climate Mode	Metric Used in Model	Source
ENSO	Niño 3.4	NOAA OOPC (2021)
IOD	Dipole Mode Index (DMI)	NOAA OOPC (2021)
TSA	Tropical South Atlantic (TSA)	NOAA OOPC (2021)
AAO	Southern Annular Mode (SAM)	NOAA CPC (2021)
MJO	Outgoing Longwave Radiation (OLR)	NOAA PSL (2021)

242 Note that there are other important modes of variability in the MSEA region that
 243 we do not include in our model, such as monsoons, wave phenomenon, diurnal patters,
 244 and tropical cyclones (Reid et al., 2012). These factors are excluded here because we solely
 245 aim to examine the connections between climate mode indices and atmospheric CO (as
 246 a proxy for fire intensity) in a higher level of detail than previous work, rather than build
 247 a comprehensive forecasting tool for the region.

248 3 Multiple Linear Regression Model

249 We use lagged multiple linear regression to model the relationship between CO anoma-
 250 lies and climate mode indices. We include first order interaction terms to capture the
 251 interconnected nature of the global climate system. Buchholz et al. (2018) found that
 252 these interaction terms were highly significant in explaining CO variability. Unlike the
 253 models in Buchholz et al. (2018), we also include squared terms to capture potential non-
 254 linear relationships between the mean CO response and the climate mode indices. For
 255 a given region, we assume that

$$256 \quad CO(t) = \mu + \sum_k a_k \chi_k(t - \tau_k) + \sum_{i,j} b_{ij} \chi_i(t - \tau_i) \chi_j(t - \tau_j) + \sum_l c_l \chi_l(t - \tau_l)^2 + \epsilon(t), \quad (1)$$

257 where $CO(t)$ is the CO anomaly at time t , μ is a constant mean offset, a_k , b_{ij} , and
 258 c_l are coefficients, χ are the climate indices, τ is the lag value for each index in weeks,
 259 $\epsilon(t)$ is a random error component, and k , i , j , and l iterate over the number of climate
 260 indices used in the analysis. Note that we standardize the climate indices, χ , before fit-
 261 ting the model so that coefficient estimates can be directly compared. We consider lags
 262 between one and 52 weeks for each index. We also enforce strong hierarchy, meaning that
 263 any covariate that appears in an interaction or squared term must also appear as a main
 264 effect. Strong hierarchy has long been recommended for models with interactions, as it
 265 helps avoid misinterpretation of the included covariates (Nelder, 1977). See the Support-
 266 ing Information file for more details on strong hierarchy.

267 Although the high frequency variability present in the weekly climate index data
 268 has important near-term effects, we do not expect it to have a large impact on the amount,
 269 type, and dryness of available fuel far into the future. This is because we believe that
 270 short anomalies do not last long enough to drastically alter large scale fuel reserves. There-

271 fore, we want covariates with longer lags to capture progressively lower frequency com-
 272 ponents of the climate indices.

273 To accomplish this, we apply more smoothing to the climate mode indices as the
 274 length of their lag in the statistical model increases. In brief, we do not smooth indices
 275 for lags below four weeks to capture as much high frequency signal as possible in these
 276 short term relationships. For lags between four and 52 weeks, we use Gaussian kernels
 277 to linearly increase the amount of smoothing applied to the indices. More information
 278 on our smoothing scheme can be found in the Supporting Information file.

279 4 Variable Selection and Model Fitting

280 We consider 52 lags of each climate mode index, quadratic terms, and all pairwise
 281 interactions, which results in far more covariates than observations. In this regime, there
 282 is not a unique least squares solution, so another model fitting method is needed to com-
 283 pute coefficient estimates. Furthermore, we want to perform variable and lag selection
 284 to obtain human-interpretable models. Buchholz et al. (2018) broke this process up into
 285 two parts. First, they iterated through all possible lag combinations. At a given com-
 286 bination of lag values, stepwise selection was used for variable selection. This resulted
 287 in a list of optimally performing models, with one model for each combination of lag val-
 288 ues. Adjusted R^2 was then used to select a single model from this list. By iterating through
 289 the lag values in this manner, Buchholz et al. (2018) was able to use stepwise selection
 290 without large computational resources. However, this strategy allowed for only a single
 291 lag of each index in the models.

292 To capture more complex relationships involving multiple lags of a given index, we
 293 instead consider all possible lags for each index simultaneously. This makes the search
 294 space too large for stepwise selection, so we instead employ regularization for both vari-
 295 able and lag selection. In the linear regression setting, regularization is a method of com-
 296 puting coefficient estimates that balances model fit and the overall magnitude of the co-
 297 efficients with the goal of finding models that generalize well to new data. Furthermore,
 298 regularization is well suited for problems with more covariates than observations, mak-
 299 ing it feasible to consider all lag values for each index simultaneously.

300 We use a flexible regularization penalty called the Minimax Concave Penalty (MCP)
 301 (Zhang, 2010). Similar to the Least Absolute Shrinkage and Selection Operator (LASSO)
 302 penalty (Tibshirani, 1996), the MCP shrinks insignificant coefficient estimates to exactly
 303 zero, which leads to interpretable models with relatively few terms. Additionally, the MCP
 304 results in less biased estimates for the remaining non-zero coefficients by allowing for larger
 305 coefficients on the significant terms (Zhang, 2010). We found that using the MCP in-
 306 stead of the LASSO improved model performance. The MCP introduces a second pa-
 307 rameter, η , that controls the MCP penalty in addition to the tuning parameter, λ , which
 308 is present in all regularization methods. The λ parameter balances how well the model
 309 fits to data and the overall magnitude of the coefficients (with a smaller overall magni-
 310 tude leading to models with less terms). Compared to the LASSO, the MCP relaxes as
 311 the coefficients get larger and plateaus after they reach a certain magnitude. The η pa-
 312 rameter controls when this plateau occurs, with smaller η values enabling larger coef-
 313 ficient estimates on the significant terms. Optimal λ and η values need to be learned from
 314 data.

315 To select parameter values, we perform a simple grid search over a range of η and
 316 λ values. We use the MCP to fit a model at each combination of η and λ values (imple-
 317 mented in R via the RAMP package from Hao et al. (2018)). We then choose between the
 318 resulting models via the Extended Bayesian Information Criterion (EBIC). The EBIC
 319 applies a much stronger penalty to large models (i.e., models with many selected terms)
 320 than other information criteria through a third parameter, γ , which is defined on the range

[0, 1]. When $\gamma = 0$, the EBIC is identical to the Bayesian Information Criterion (BIC), but when $\gamma = 1$, the EBIC is much harsher than the BIC. This is well suited for applications in which the number of possible covariates is large, but the optimal model might in fact be quite small. Since the number of potential covariates in this application is vast (recall that each lag value represents a different covariate), we use the EBIC rather than the BIC to select the final model. After finalizing the model terms in this manner, we refit their coefficient estimates via maximum likelihood.

More details on regularization, the MCP, the EBIC, and how we select parameter values can be found in the Supporting Information file. In the remaining sections, we discuss how this modeling framework and the choice of γ can be used to address our two goals of model interpretability and predictive performance.

5 Interpreting Fitted Models

Here we examine the physical implications of the models fit using the procedure described in Section 4. We focus on connections between climate and CO in MSEA through an analysis of selected indices and lag values.

5.1 A Framework for Identifying Optimally Performing Models at Various Complexities

We can create a list of “optimally performing” models at decreasing complexities (i.e., number of terms) by increasing the EBIC parameter, γ , on the range $[0, 1]$, as larger γ values increase the penalty on large models. Optimal here refers to the fact that these models are the result of a grid search over the other two free parameters, λ and η . For MSEA, this procedure results in the models listed in Figure 4. The color of each box corresponds to the γ value that was used to generate the model contained within it. Note that multiple γ values can produce the same model. Within each box, the name of the index and the corresponding lag is listed (in the format “`name_lag`”), along with the coefficient estimates and standard errors.

Moving from left to right in Figure 4, we see that the models decrease in size (from 17 terms to nine), while their performance drops only slightly (from adjusted R^2 of 0.68 to 0.60). By examining the terms that remain in the model as it becomes more parsimonious, we can determine which indices and lags are most influential in explaining variability in the response.

For MSEA, we can see that the Niño 3.4 index lagged at four weeks remains in the model with a positive coefficient estimate. This makes sense, as ENSO is a major climate driver in the tropics, with positive anomalies resulting in warmer, drier conditions (Nur’utami & Hidayat, 2016). The lag of four weeks indicates that it takes about four weeks for the effect of a Niño 3.4 anomaly to impact CO anomalies. Additionally, the Niño 3.4 lag of four weeks appears as a squared term in the most parsimonious model, indicating that there is a nonlinear relationship between Niño 3.4 and CO. This is confirmed by examining the residuals of a model fit to solely the Niño 3.4 lag of four weeks (not shown).

The selected DMI lags also suggest an interesting relationship. Note that positive DMI anomalies are associated with reduced rainfall in parts of MSEA, while negative DMI anomalies are associated with increased rainfall (Nur’utami & Hidayat, 2016). A DMI lag of 12 weeks remains in the model as it becomes more parsimonious, as well as a shorter lag that switches from one to four weeks between the smallest two models. The coefficient on the longer lag is negative, while the coefficient on the shorter lag is positive. The coefficient on the shorter lag implies that reduced rainfall (i.e., positive DMI anomalies) results in more CO on average, and vice versa. This is likely the result of an

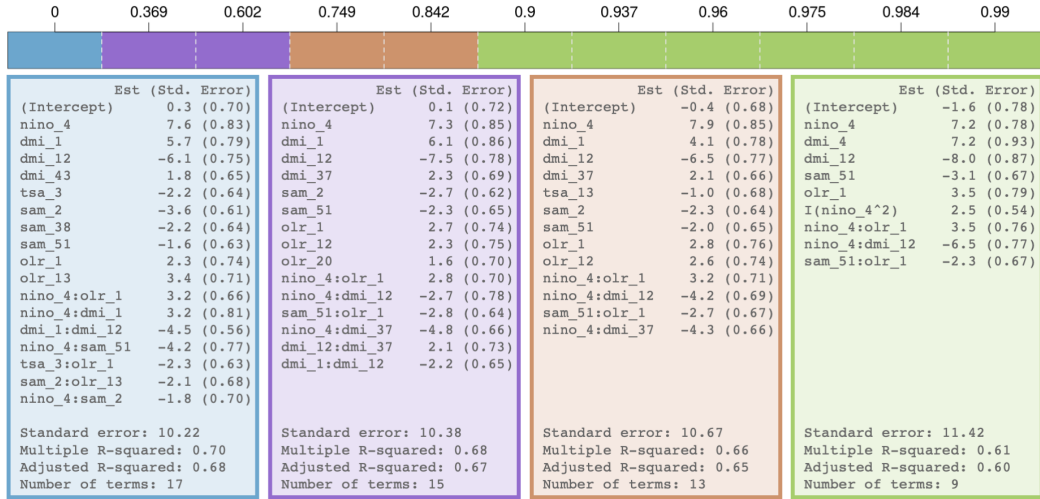


Figure 4. Optimal models for the MSEA region for a logarithmic sequence of γ values. Note that multiple γ values can produce the same model. The color of each box corresponds to the γ value that was used to generate the model contained within it. The model terms are listed in the format “name_lag,” where lags are in weeks. Interaction terms are listed in the format “name1_lag1:name2_lag2.” Coefficient estimates and standard errors are listed for each term, and summary statistics are listed below each model. Note that “nino” refers to the Niño 3.4 index.

intuitive relationship: reduced rainfall leads to drier conditions that are more prone to burning (and hence more CO). Similar to the ENSO relationship, these dry conditions take one to four weeks to impact CO. The coefficient on the longer lag, however, implies the opposite: reduced rainfall (i.e., positive DMI anomalies) results in less CO on average, and conversely, increased rainfall results in more CO on average. This could be because rainfall leads to vegetation growth, which ultimately provides more fuel for fires. The length of this lag is longer, implying that it takes around 12 weeks for the increased vegetation growth to impact CO concentrations.

The effect of these two DMI lags is compounding. That is, more vegetation from DMI-driven rainfall at a 12 week lead time results in more fuel for burning when a subsequent positive DMI anomaly drives drier conditions. This is supported by the negative coefficient on the interaction between the DMI lag of 12 weeks and one week present in the largest model in Figure 4. Because the coefficient is negative, there is less CO on average when the DMI has the same phase (i.e., either a positive or negative anomaly) at both a 12 and one week lag.

An OLR term lagged at one week remains in the MSEA model as it becomes more parsimonious with a positive coefficient estimate. This again makes sense, as positive OLR anomalies are associated with less cloud cover and hence less rain. The one week lag suggests that an OLR-driven decrease in rain leads to more CO in the short term, likely as a result of increased burning. The TSA index, on the other hand, is only included in the largest model. This could be because the TSA describes sea surface temperatures in the southern Atlantic Ocean, which is very far from MSEA. Therefore, it makes sense that the TSA is less important than the other indices in explaining CO variability in MSEA, as the other indices are based on aspects of the global climate system located closer to MSEA.

394 Finally, two Niño 3.4 interaction terms remain in the model as it becomes more par-
 395 simonious. One interaction is with the OLR at a one week lag and the other is with the
 396 DMI at a 12 week lag. The sign of these interaction terms is the same as the non-Niño
 397 3.4 component. This indicates that the effects of these indices are amplified when they
 398 are in phase, a result that has been previously identified in the literature (Cleverly et
 399 al., 2016; Nur’utami & Hidayat, 2016). Note that studies like Islam et al. (2018) have
 400 shown that there is increased fire potential when Niño 3.4 and DMI are both positive.
 401 Our model agrees with this finding (see the Niño - DMI interaction in the largest model),
 402 but also expands on this finding by showing that Niño also amplifies the effect of DMI
 403 at longer lead times (see the Niño - DMI interaction in the smallest model). Our results
 404 are also consistent with Reid et al. (2012), who show that an increase in fire activity oc-
 405 curs during the ENSO warm phase and positive IOD phase. Reid et al. (2012) also found
 406 evidence of a relationship between ENSO and IOD. We expand on this work by spec-
 407 ifying the Niño 3.4 and DMI lead times that most significantly influence CO and by show-
 408 ing how the Niño - DMI interaction changes at different lead times.

409 These findings largely agree and expand upon the results in Buchholz et al. (2018).
 410 For MSEA, Buchholz et al. (2018) found that a Niño 3.4 lag of one month, DMI lag of
 411 eight months, TSA lag of five months, and SAM lag of one month were important pre-
 412 dictors. The largest model presented in this study contains a Niño 3.4 lag of four weeks,
 413 DMI lag of 43 weeks, TSA lag of three weeks, and SAM lag of two weeks. All but the
 414 TSA term (which we will show to be less important for MSEA in Section 5.2) agree closely
 415 on their selected lag. However, the models we present here are capable of including mul-
 416 tiple lags of a single index, which expands on the work in Buchholz et al. (2018) and high-
 417 lights more complex relationships between climate and CO.

418 5.2 Assessing Stability of Selected Model Terms

419 While the scientific conclusions drawn in the previous section seem to agree with
 420 and expand upon current literature, we want to ensure that the selected covariates are
 421 in fact meaningful. That is, we want to avoid over-interpreting the role of covariates if
 422 slight changes in data result in drastically different models, as these models would not
 423 be capturing a meaningful physically-based relationship but would rather be artifacts
 424 of the specific training data.

425 Therefore, we perform one-year-out resampling to assess the stability of selected
 426 covariates. We perform the resampling on the largest model from Figure 4 because it con-
 427 tains most of the terms present in the smaller models. Specifically, we perform the fol-
 428 lowing resampling procedure. We first iterate through the years present in the data. For
 429 each year, we create a testing set containing all data falling within that year and a train-
 430 ing set containing the remainder of the data. We then train two models using only data
 431 from the training set. We force the first model (called the “constant structure model”)
 432 to retain the same covariates as the model trained on all of the data but allow for dif-
 433 ferent coefficient estimates. We let the second model (called the “varying structure model”)
 434 to completely change based on the particular training set, meaning that it can have dif-
 435 ferent covariates and coefficient estimates than the model trained on all of the data. We
 436 then test these two models on the corresponding test set and compute the root mean square
 437 error (RMSE) for both.

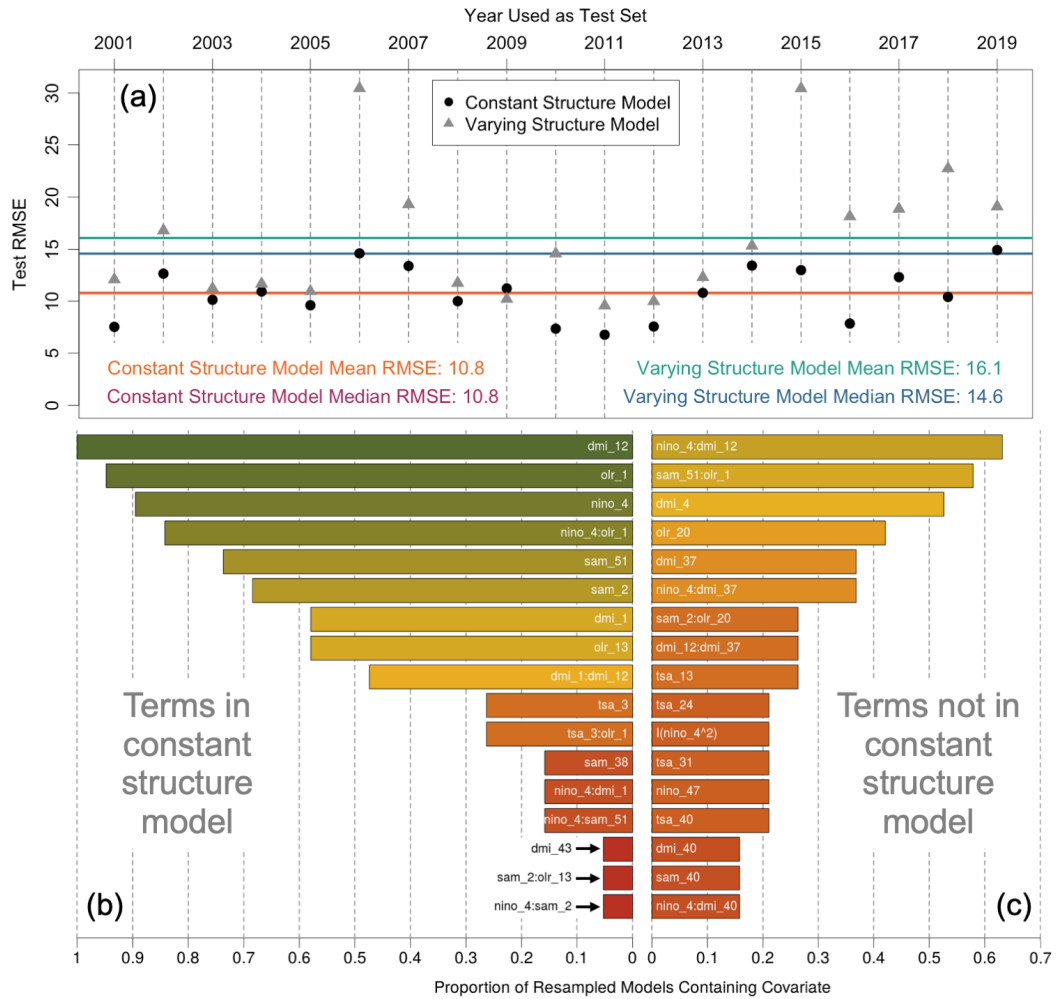


Figure 5. Results from the one-year-out resampling. Constant structure model refers to the model forced to retain the structure of the model trained on all of the data, but with refit coefficient estimates. New model refers to the model allowed to completely change according to the particular training set. (a) shows the out-of-sample prediction error for each testing set. The year on the horizontal axis indicates which year was used to test the models. The constant structure model almost always outperforms the varying structure model. (b) shows the frequency with which constant structure model terms appear in the varying structure models. Similarly (c) shows the frequency with which terms not present in the constant structure model appear in the varying structure model. The most significant covariates from Figure 4 appear in many of the retrained models. The color in (b) and (c) corresponds to the proportion on the horizontal axis and is included for visual clarity. Note that “nino” refers to the Niño 3.4 index.

438 Figure 5 shows the results of this resampling and is divided into three sections. Fig-
 439 ure 5(a) shows the out-of-sample prediction error (RMSE) from both models for each
 440 training set. The year on the horizontal axis corresponds to the year reserved for the test-
 441 ing set. The RMSE of the constant structure model tends to perform as well or better
 442 than the varying structure model. This provides justification for using the form of the
 443 model trained on all data as the representative model for MSEA and further interpret-
 444 ing its covariates, as the relationships captured by this model do a better job at explain-
 445 ing the data than those in the varying structure models. Note that the RMSE of the vary-

ing structure model is largest when 2006 and 2015 are left out of the training set. These years contained some of the largest CO anomalies of the 19 year time series (see Figure 2). This indicates that: 1) these extreme fire years are important in driving the form of the model trained on all data, and 2) this framework should be used with caution in a forecasting setting.

Figure 5(b) and Figure 5(c) show how often certain terms appear in the varying structure models (that is, the models allowed to completely change according to the new training data). This gives some indication of the stability of the various model terms. If a term is present in many of the retrained models, then the modeling framework is likely picking up a physically-based relationship. Terms that are absent from many of the retrained models are more likely artifacts of the specific training set, rather than a true physical relationship.

Figure 5(b) shows how often the constant structure model terms reappear in the varying structure models. Notably, the terms present in the most parsimonious model from Figure 4 are most likely to appear in the retrained models. This indicates that these terms are explaining the most stable aspect of the physical relationship. Other terms, such as the 43 week DMI lag, rarely appear in the retrained models. This indicates that less consideration should be given to these terms when attempting to explain the physical relationship between climate and CO.

Figure 5(c) shows how often terms not present in the constant structure model appear in the retrained models. Note the different scales on the horizontal axis between subfigures 5(b) and 5(c). In Figure 5(c) we see that a selection of terms not in the constant structure model appear relatively frequently in the retrained models. Recall that when moving from the second smallest to the smallest model in Figure 4, the shorter DMI lag switches from one week to four weeks. In Figures 5(b) and (c), we see that both the one and four week DMI lags show up in about half of the retrained models. This indicates that these terms are interchangeable, and determining which is included likely depends on the other selected covariates.

Figures 5(b) and (c) further confirm that the terms present in the most parsimonious model for the region (see Figure 4) are capturing meaningful signal and are not simply artifacts of the specific training set. This is because these terms remain in a large majority of the retrained models, each of which is trained on a different subsample of the data. Furthermore, Figure 5(c) illustrates that the interaction between Niño 3.4 lagged at four weeks and DMI lagged at 12 weeks, although not present in the constant structure model, is still a significant interaction in explaining CO variability in MSEA. This also holds for the interaction between SAM lagged at 51 weeks and OLR lagged at one week. The terms that are included less often in the retrained models are likely more data dependent and help the model capture subtleties in the response. As a result, it is more likely that these terms would change with small changes in the data. An example is the TSA term lagged at three weeks present in the constant structure model. This term appears in less than 30% of the retrained models, which confirms the analysis in Section 5.1 that finds that TSA is less important in explaining CO variability in MSEA.

The stability analysis presented here provides further justification for assigning scientific weight to selected model terms, as it shows that certain stable terms are not simply artifacts of the particular training set used to fit the model. In particular, we confirm that a number of terms from the smallest model presented in Figure 4 are very stable: DMI lagged at 12 weeks, OLR lagged at one week, Niño 3.4 lagged at four weeks, a short DMI lag (of either one or four weeks depending on the remaining model terms), SAM lagged at 51 weeks, the interaction between Niño 3.4 lagged at four weeks and OLR lagged at one week, and the interaction between Niño 3.4 lagged at four weeks and DMI lagged at 12 weeks. This provides further evidence that these terms specify the most significant relationships between climate and atmospheric CO in MSEA.

6 Assessing Model Predictions

We now turn our attention to the predictive performance of selected models. We again focus on the largest model from Figure 4, as this model has the best predictive capabilities. Strong predictive performance indicates that there is indeed a connection between climate mode indices and CO variability and that our model is able to capture part of this connection. Therefore, strong predictive performance gives additional weight to the scientific interpretation of the selected model terms. Note that the performance metrics discussed in this section (e.g., percent of variability explained) are not meant to be an assessment of our model’s forecasting ability, but rather an assessment of how well we can explain the response (CO variability) using only our predictors (climate mode indices).

6.1 Model Predictions with No Minimum-Lag-Threshold

In this subsection we impose no requirements on the minimum lag value allowed in the models, meaning that we allow lags of one to 52 weeks as in Figure 4. In Figures 6 and 7 we demonstrate the predictive capabilities of our model and highlight two interesting results.

Figure 6 shows weekly observations and predictions from two model variants. Note that these predictions are in-sample, meaning that they are predictions of the observations used to train the model. The top plot of Figure 6(a) shows predictions from a model completely refit to a data set excluding the OLR, and the bottom plot shows predictions from the full model (i.e., the model presented in Figure 4). We can see that including the OLR results in a slight decrease in RMSE and increase in both R^2 and adjusted R^2 . Note that adjusted R^2 is a better metric for comparing the two models, as it accounts for the number of terms in each model. Similar to R^2 , higher adjusted R^2 values indicate a better fit. Furthermore, in Figure 6(b) and (c), we highlight two of the most anomalous years, which shows that the OLR helps capture the extreme CO anomalies. This makes sense for 2015 in particular, as the MJO and our OLR proxy experienced an extreme anomaly during this year.

Figure 7 shows month-averaged observations and predictions from two different model variants. The top plot of Figure 7(a) shows predictions from a month-based model. To create this model, we took month-averages of the predictor variables and then trained the model on only these month-averaged covariates using the framework presented in Section 4. We imposed no restrictions on the terms included in this model, as we do not want to introduce information from the weekly data that would not otherwise be available in the monthly data. The bottom plot shows month-averaged predictions from the model trained on weekly data (i.e., the model shown in Figure 4). We see a noticeable increase in model performance when using the weekly data, suggesting that the weekly data is able to capture meaningful signal beyond the month-averages. This is an interesting result, as it suggests that the higher frequency signals present in the climate indices are in fact meaningful signal and not simply noise. This is perhaps most important for OLR (the proxy for localized MJO), which has a higher frequency component than the other included climate indices. This increase in performance can be seen clearly during the 2015 CO anomaly.

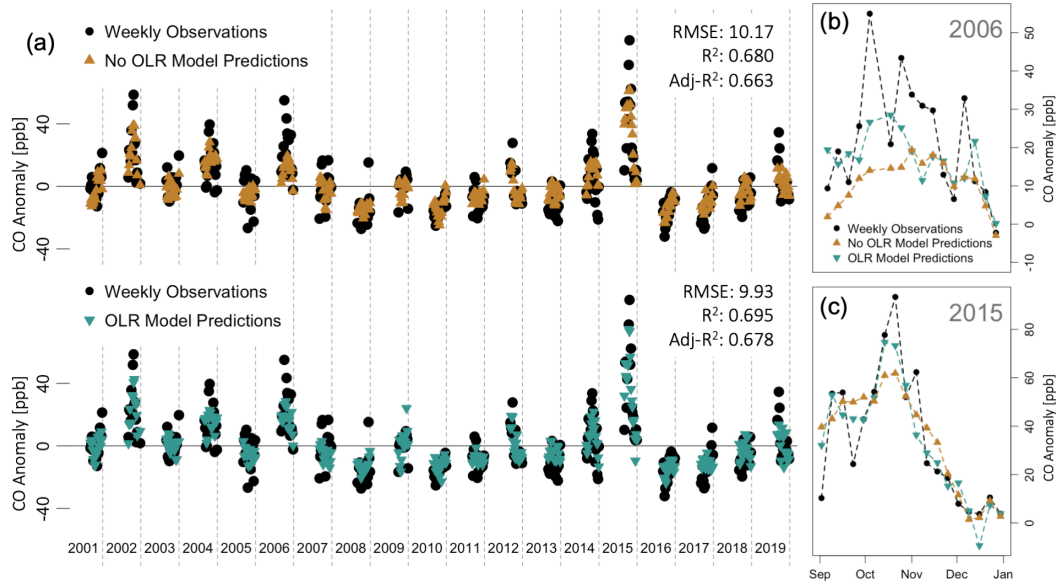


Figure 6. In-sample predictions from two model variants. In (a), the top plot shows predictions from the optimal model without the OLR, and the bottom plot shows predictions from the optimal model with the OLR. Adding the OLR appears to increase predictive performance during the extreme CO anomalies shown in (b) and (c).

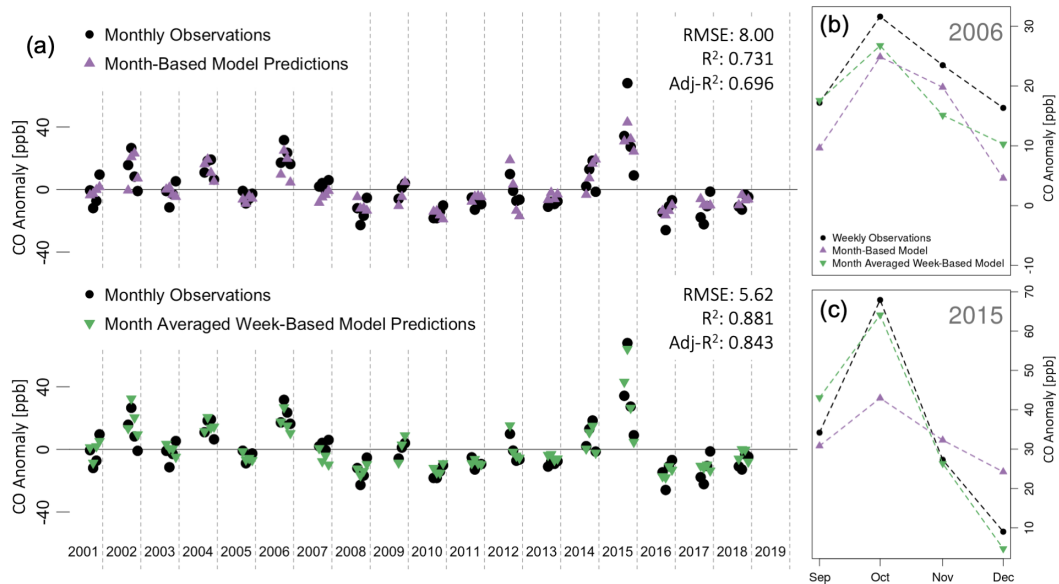


Figure 7. In-sample predictions from two additional model variants. In (a), the top plot shows predictions from a model trained on month-averaged covariates, and the bottom plot shows month-averaged predictions from a model trained on week-averaged covariates. The increase in model performance indicates that there is meaningful signal in the higher frequency climate index data, which is clearly seen in the anomalous years shown in (b) and (c).

541 Note that the predictions from these models are an improvement over the models
 542 in Buchholz et al. (2018). When using week-averaged data to train the model, we are
 543 able to explain 88% of the variability in the month-averaged CO observations. The model
 544 in Buchholz et al. (2018) explains 75% of the month-averaged CO. This increase in pre-
 545 dictive performance is likely a result of: 1) the ability to include multiple lags of a sin-
 546 gle climate mode index, 2) the additional signal contained in the week-averaged data,
 547 and 3) the inclusion of the OLR proxy index.

548 6.2 Increasing Minimum-Lag-Threshold

549 The predictions shown in Subsection 6.1 are useful for demonstrating model per-
 550 formance and the comparative benefit of using the OLR and week-averaged data. How-
 551 ever, these models include an OLR term lagged at one week (see Figure 4), which means
 552 that they can only be used to forecast one week ahead. In this section, we explore the
 553 capabilities of our model in a more practical forecasting environment. Note that we are
 554 not attempting to outperform or even match state-of-the-art forecasting tools that uti-
 555 lize modes of variability beyond just climate modes. Instead, we are interested in explor-
 556 ing the forecasting performance of our statistical model trained solely on climate mode
 557 indices, which will potentially help forecasters attempting to build more sophisticated
 558 tools.

559 To increase the prediction horizon, we implement a minimum-lag-threshold that
 560 only allows lags greater than the threshold value to be included in the model. Because
 561 increasing this threshold reduces the number of possible covariates, we also extend the
 562 maximum lag value as the minimum-lag-threshold is increased. Specifically, we consider
 563 lags between the minimum-lag-threshold and 52 weeks plus this threshold. This ensures
 564 that all models are based on one year of climate data, making it easier to compare their
 565 predictive performance.

566 Figure 8 shows a selection of model performance metrics as this minimum-lag-threshold
 567 is increased. We focus on the largest model generated from the range of EBIC γ values,
 568 as this model has the best predictive performance. The top plot in Figure 8 shows the
 569 number of terms in the selected model for each minimum-lag-threshold. The second plot
 570 shows the adjusted R^2 value of the selected models. As expected, the model performance
 571 drops off as the minimum lag is increased. However, this decline is not very rapid. That
 572 is, models with a high minimum-lag-threshold still explain a large percent of the vari-
 573 ability in atmospheric CO anomalies. This is promising, as it means that predictions can
 574 be made farther in advance without losing too much predictive performance. The third
 575 plot shows another performance metric: the average out-of-sample prediction error from
 576 one-year-out resampling. Here we successively leave one year out, train the model on the
 577 remaining data, and test it on the left out year. The average RMSE is then taken for
 578 each different training and testing set pair and plotted as a function of minimum-lag-
 579 threshold. We see that performance falls off, although gradually.

580 We think that the gradual nature of the decline in model performance is a result
 581 of the climate indices exhibiting high auto-correlation (not shown). Since many of the
 582 short lags are highly correlated to longer lags of the same index, we think that these longer
 583 lags are able to explain much of the same CO variability when the shorter lags are ex-
 584 cluded. This is again promising, as it means that predictions can be made decently far
 585 in advance (on the order of a half year) without dramatically compromising performance.

586 To further visualize model performance at increasingly large minimum-lag-thresholds,
 587 we consider predictions for the 2015 CO event in MSEA. Figure 9 shows predictions from
 588 the models corresponding to the minimum-lag-thresholds from Figure 8. The predictions
 589 largely capture the structure of the CO observations for minimum-lag-thresholds below
 590 25 weeks (about six months). After this point, the predictions begin to flatten out (i.e.,
 591 not capture the extremes in the response) and the predicted spike starts earlier in the

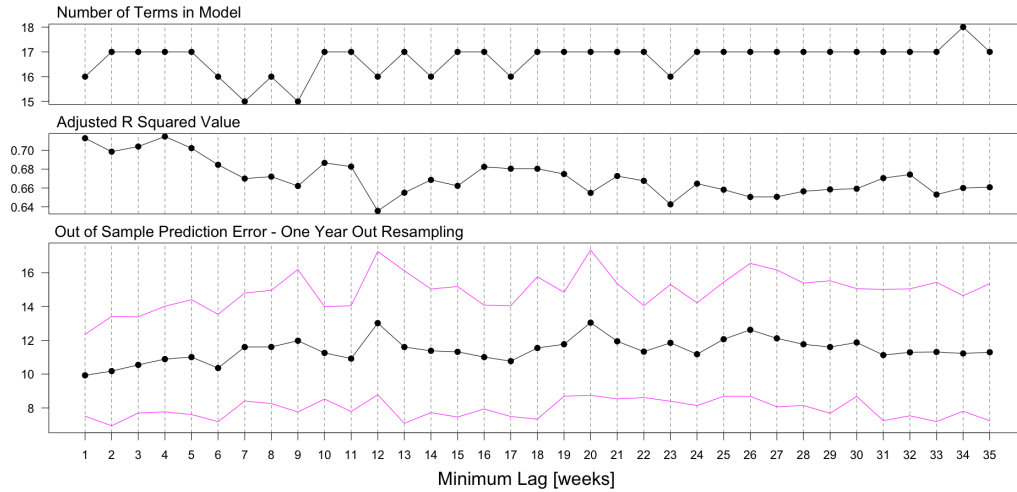


Figure 8. Model performance for MSEA at increasing minimum-lag-thresholds. Top plot shows the number of terms in the selected model. Middle plot shows the adjusted R^2 value of the selected model. Bottom plot shows an average out-of-sample prediction error for each model with magenta lines showing \pm one standard deviation. Here we iteratively leave one year out, train the model on the remaining data, and test it on the left out year. Plotted is the average RMSE with \pm one standard deviation lines in magenta from this procedure as a function of minimum lag. We can see that model performance drops off with an increasing minimum-lag-threshold, although at a fairly gradual pace.

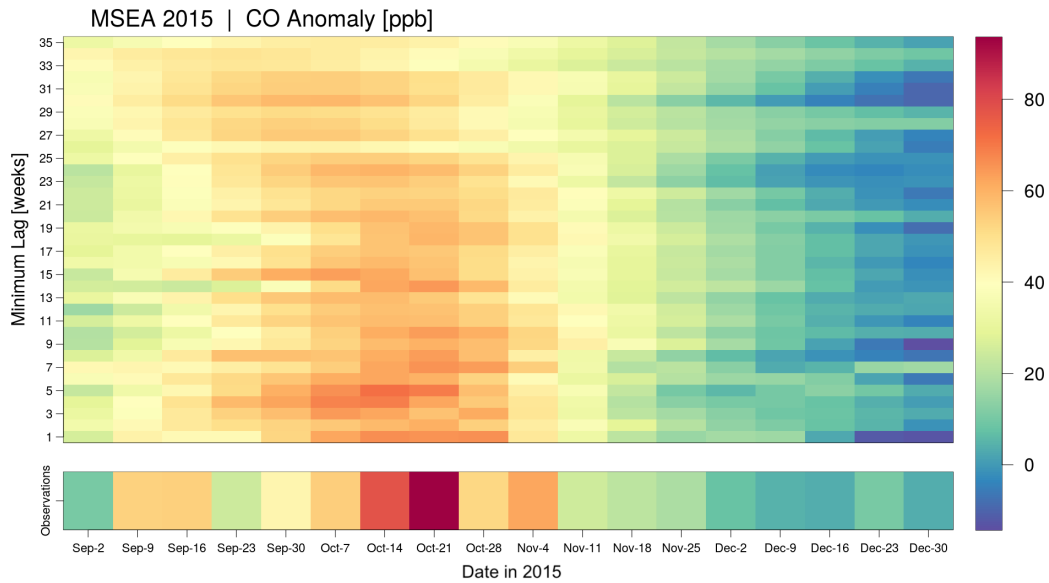


Figure 9. Predictions of the 2015 CO anomalies [ppb] in MSEA for a range of minimum-lag-thresholds. Color represents CO anomalies, and the horizontal axis represents time. MOPITT observations are shown as a horizontal bar along the bottom of the figure. The remaining vertical axis corresponds to the minimum-lag-threshold used to fit the model, and hence each row of the figure contains predictions from a different model. The minimum-lag-threshold can be interpreted as the prediction horizon of the model. We see that the general structure of the observed CO anomalies is preserved for minimum lags under 25 weeks (about half a year).

592 year (i.e., in early September instead of early October). This result largely agrees with
 593 Shawki et al. (2017), who found that a drought metric could be reasonably predicted 180
 594 days (about 25 weeks) in advance. However, unlike Shawki et al. (2017), our predictions
 595 rely solely on past climate mode index anomalies, rather than forecasts from a global cli-
 596 mate model.

597 7 Summary

598 We build on previous work aimed at explaining the relationship between climate
 599 and atmospheric CO variability. Atmospheric CO is a useful proxy for fire intensity, as
 600 fires are the main source of CO variability in the Southern Hemisphere and CO is remotely
 601 sensed on a global scale.

602 Our proposed regularization framework highlights a variety of optimally perform-
 603 ing models at decreasing complexities, isolating the most important indices and lag val-
 604 ues as the models become more parsimonious. For MSEA, we identify the Niño 3.4 in-
 605 dex lagged at four weeks as a primary driver of atmospheric CO. Other important cli-
 606 mate indices are the DMI and OLR (as a proxy for the MJO). We further identify that
 607 Niño 3.4 interactions with the OLR and DMI are significant predictors, suggesting that
 608 the effect of these indices is amplified when they are in phase. Finally, we show that in-
 609 cluding multiple lags of the DMI is important for explaining CO variability in MSEA.
 610 While these results broadly agree with current literature, we go beyond the usual treat-
 611 ment of climate mode indices on a seasonal time scale by identifying the specific weekly
 612 lead times for each index that have the most influence on CO variability.

613 We also perform a resampling-based sensitivity analysis to quantify the robustness
 614 of the model fit to all data. We find that the model forced to retain the covariates from
 615 the model trained on all data performs as well or better than the model allowed to com-
 616 pletely change based on the training set. This provides justification for using the mod-
 617 els from Figure 4 as the representative models for MSEA. Additionally, we determine
 618 which covariates are most likely to remain in the model when trained on slightly differ-
 619 ent data, finding that the terms in the most parsimonious model from Figure 4 are also
 620 the most robust. This justifies assigning scientific weight to the selection of these terms,
 621 as it suggests that they are capturing a physically-based relationship and are not sim-
 622 ply artifacts of the specific training set used.

623 We show that our model for the MSEA region can explain around 70% of the vari-
 624 ability in the weekly CO anomalies solely using climate indices as predictor variables.
 625 We further use model predictions to highlight the importance of the OLR (as a proxy
 626 for the MJO) in overall model performance and in explaining the most extreme CO anoma-
 627 lies. Similarly, we show that month-averaged predictions from a model trained on week-
 628 averaged data outperform predictions from a model trained on month-averaged data. This
 629 suggests that there is meaningful signal in the week-averaged data and justifies its use
 630 over month-averaged data. Note that the predictions from these models are an improve-
 631 ment over those in Buchholz et al. (2018), as they explain 88% of the variability in month-
 632 averaged CO observations compared to 75%.

633 Finally, we perform a minimum-lag-threshold study to assess the performance of
 634 our model in a forecasting setting. We find that models for MSEA are still able to ex-
 635 plain around 65% of the weekly atmospheric CO variability when forced to only use lags
 636 greater than 35 weeks. While we do not attempt to outperform or even match state-of-
 637 the-art forecasting tools, we believe that this information is useful to forecasters hop-
 638 ing to maximize the information they glean from climate modes when developing more
 639 sophisticated tools.

640 Overall, we believe that our modeling framework quantifies the relationship between
 641 climate mode indices and atmospheric CO (as a proxy for fire intensity and as a mea-

642 sure of air quality) at a level of complexity not previously studied. We do this by uti-
 643 lizing climate mode indices on a weekly timescale, accommodating multiple lead times
 644 of each climate mode, and including complex interactions between climate mode indices
 645 at a weekly timescale. We believe that this work will be useful for scientists studying modes
 646 of variability in MSEA.

647 Acknowledgments

648 The NCAR MOPITT project is supported by the National Aeronautics and Space Ad-
 649 ministration (NASA) Earth Observing System (EOS) Program. The MOPITT team also
 650 acknowledges support from the Canadian Space Agency (CSA), the Natural Sciences and
 651 Engineering Research Council (NSERC) and Environment Canada, and the contribu-
 652 tions of COMDEV and ABB BOMEM. The National Center for Atmospheric Research
 653 (NCAR) is sponsored by the National Science Foundation.

654 Open Research

655 MOPITT carbon monoxide data are publicly available through NASA. See
 656 <https://doi.org/10.5067/TERRA/MOPITT/MOP02J.L2.008>. Climate index data are pro-
 657 duced and maintained by NOAA. See <https://stateoftheocean.osmc.noaa.gov> and
 658 <http://www.cpc.ncep.noaa.gov>. Only a subset of the MOPITT V8 Level 2 carbon monox-
 659 ide data is used in this work. The processed carbon monoxide and climate mode index
 660 data used in this work are publicly available through NCAR. See
 661 <https://doi.org/10.5065/s6rv-rc57> (Buchholz, Worden, Ahamad, et al., 2021). The
 662 R code used to implement the model fitting framework proposed in this work can be ac-
 663 cessed through GitHub. See <https://github.com/wsdaniels/C0modeling>.

664 References

- 665 Alencar, A., Asner, G. P., Knapp, D., & Zarin, D. (2011). Temporal variability
 666 of forest fires in eastern Amazonia. *Ecological Applications*, *21*(7), 2397–2412.
 667 doi: 10.1890/10-1168.1
- 668 Andela, N., & van der Werf, G. R. (2014). Recent trends in African fires driven by
 669 cropland expansion and El Niño to la Niña transition. *Nature Climate Change*,
 670 *4*(9), 791–795. doi: 10.1038/nclimate2313
- 671 Andreoli, R. V., & Kayano, M. T. (2006). Tropical Pacific and South Atlantic effects
 672 on rainfall variability over Northeast Brazil. *International Journal of Climatol-*
 673 *ogy*, *26*(13), 1895–1912. doi: 10.1002/joc.1341
- 674 Bamston, A. G., Chelliah, M., & Goldenberg, S. B. (1997). Documentation of a
 675 highly ENSO-related sst region in the equatorial pacific: Research note. *Atmo-*
 676 *sphere - Ocean*, *35*(3), 367–383. doi: 10.1080/07055900.1997.9649597
- 677 Bien, J., Taylor, J., & Tibshirani, R. (2013). A lasso for hierarchical interactions.
 678 *The Annals of Statistics*, *41*(3), 1111–1141. doi: 10.1214/13-AOS1096
- 679 Birch, C. E., Webster, S., Peatman, S. C., Parker, D. J., Matthews, A. J., Li, Y.,
 680 & Hassim, M. E. E. (2016). Scale interactions between the MJO and the
 681 Western Maritime Continent. *Journal of Climate*, *29*, 2471–2492. doi:
 682 10.1175/JCLI-D-15-0557.1
- 683 Bloom, A. A., Worden, J., Jiang, Z., Worden, H., Kurosu, T., Frankenberg, C., &
 684 Schimel, D. (2015). Remote-sensing constraints on South America fire traits by
 685 Bayesian fusion of atmospheric and surface data. *Geophysical Research Letters*,
 686 *42*(4), 1268–1274. doi: 10.1002/2014GL062584
- 687 Breheny, P., & Huang, J. (2011). Coordinate descent algorithms for nonconvex pe-
 688 nalized regression, with applications to biological feature selection. *The Annals*
 689 *of Applied Statistics*, *5*(1), 232–253. doi: 10.1214/10-AOAS388
- 690 Buchholz, R. R., Hammerling, D., Worden, H. M., Deeter, M. N., Emmons, L. K.,

- 691 Edwards, D. P., & Monks, S. A. (2018). Links between carbon monoxide
692 and climate indices for the Southern Hemisphere and tropical fire regions.
693 *Journal of Geophysical Research: Atmospheres*, *123*(17), 9786–9800. doi:
694 10.1029/2018JD028438
- 695 Buchholz, R. R., Worden, H. M., Ahamad, F., Daniels, W. S., & Hammerling,
696 D. M. (2021). *Weekly carbon monoxide anomalies over maritime southeast
697 asia and weekly climate indices*. (Version 1.0. UCAR/NCAR - GDEX) doi:
698 10.5065/s6rv-rc57
- 699 Buchholz, R. R., Worden, H. M., Park, M., Francis, G., Deeter, M. N., Edwards,
700 D. P., . . . Kulawik, S. S. (2021). Air pollution trends measured from
701 Terra: CO and AOD over industrial, fire-prone, and background regions.
702 *Remote Sensing of Environment*, *256*, 112275. doi: [https://doi.org/10.1016/
703 j.rse.2020.112275](https://doi.org/10.1016/j.rse.2020.112275)
- 704 Ceccato, P., Nengah Surati Jaya, I., Qian, J. H., Tippet, M. K., Robertson, A. W.,
705 & Someshwar, S. (2010). *Early warning and response to fires in Kaliman-
706 tan, Indonesia* (Tech. Rep.). International Research Institute for Climate and
707 Society.
- 708 Chen, Y., Morton, D. C., Andela, N., Giglio, L., & Randerson, J. T. (2016). How
709 much global burned area can be forecast on seasonal time scales using sea
710 surface temperatures? *Environmental Research Letters*, *11*(4), 45001. doi:
711 10.1088/1748-9326/11/4/045001
- 712 Chen, Y., Morton, D. C., Andela, N., van der Werf, G. R., Giglio, L., & Rander-
713 son, J. T. (2017). A pan-tropical cascade of fire driven by El Niño/Southern
714 Oscillation. *Nature Climate Change* *2017 7:12*, *7*, 906–911. doi: 10.1038/
715 s41558-017-0014-8
- 716 Cleverly, J., Eamus, D., Luo, Q., Coupe, N. R., Kljun, N., Ma, X., . . . Huete, A.
717 (2016). The importance of interacting climate modes on Australia’s contri-
718 bution to global carbon cycle extremes. *Scientific Reports*, *6*(1), 1–10. doi:
719 10.1038/srep23113
- 720 Deeter, M. N., Edwards, D. P., Francis, G. L., Gille, J. C., Mao, D., Martínez-
721 Alonso, S., . . . Andreae, M. O. (2019). Radiance-based retrieval bias mit-
722 igation for the MOPITT instrument: The version 8 product. *Atmospheric
723 Measurement Techniques*, *12*(8), 4561–4580. doi: 10.5194/amt-12-4561-2019
- 724 Deeter, M. N., Edwards, D. P., Gille, J. C., & Drummond, J. R. (2007). Sensitivity
725 of MOPITT observations to carbon monoxide in the lower troposphere. *Jour-
726 nal of Geophysical Research*, *112*(D24), D24306. doi: 10.1029/2007JD008929
- 727 Deeter, M. N., Martínez-Alonso, S., Edwards, D. P., Emmons, L. K., Gille, J. C.,
728 Worden, H. M., . . . Wofsy, S. C. (2014). The MOPITT Version 6 product: Al-
729 gorithm enhancements and validation. *Atmospheric Measurement Techniques*,
730 *7*(11), 3623–3632. doi: 10.5194/amt-7-3623-2014
- 731 Dias, J., Sakaeda, N., Kiladis, G. N., & Kikuchi, K. (2017). Influences of the MJO
732 on the space-time organization of tropical convection. *Journal of Geophysical
733 Research: Atmospheres*, *122*, 8012–8032. doi: 10.1002/2017JD026526
- 734 Drummond, J. R., Zou, J., Nichitui, F., Kar, J., Deschambaut, R., & Hack-
735 ett, J. (2010). A review of 9-year performance and operation of the
736 MOPITT instrument. *Advances in Space Research*, *45*, 760–774. doi:
737 10.1016/J.ASR.2009.11.019
- 738 Edwards, D. P., Emmons, L. K., Gille, J. C., Chu, A., Attié, J.-L., Giglio, L., . . .
739 Drummond, J. R. (2006). Satellite-observed pollution from Southern Hemi-
740 sphere biomass burning. *Journal of Geophysical Research*, *111*(D14), D14312.
741 doi: 10.1029/2005JD006655
- 742 Edwards, D. P., Pétron, G., Novelli, P. C., Emmons, L. K., Gille, J. C., & Drum-
743 mond, J. R. (2006). Southern Hemisphere carbon monoxide interan-
744 nual variability observed by Terra/Measurement of Pollution in the Tropo-
745 sphere (MOPITT). *Journal of Geophysical Research*, *111*, D16303. doi:

- 746 10.1029/2006JD007079
 747 Enfield, D. B., Mestas-Nuñez, A. M., Mayer, D. A., & Cid-Serrano, L. (1999). How
 748 ubiquitous is the dipole relationship in tropical Atlantic sea surface tempera-
 749 tures? *Journal of Geophysical Research: Oceans*, *104*(C4), 7841–7848. doi:
 750 10.1029/1998jc900109
- 751 Fonseca, M. G., Anderson, L. O., Arai, E., Shimabukuro, Y. E., Xaud, H. A. M.,
 752 Xaud, M. R., ... Aragão, L. E. O. C. (2017). Climatic and anthropogenic
 753 drivers of northern Amazon fires during the 2015–2016 El Niño event. *Ecologi-
 754 cal Applications*, *27*, 2514–2527. doi: 10.1002/EAP.1628
- 755 Fuller, D. O., & Murphy, K. (2006). The ENSO-fire dynamic in insular Southeast
 756 Asia. *Climatic Change*, *74*(4), 435–455. doi: 10.1007/s10584-006-0432-5
- 757 Giglio, L., Boschetti, L., Roy, D. P., Humber, M. L., & Justice, C. O. (2018). The
 758 Collection 6 MODIS burned area mapping algorithm and product. *Remote
 759 Sensing of Environment*, *217*, 72–85. doi: 10.1016/j.rse.2018.08.005
- 760 Giglio, L., Csiszar, I., & Justice, C. O. (2006). Global distribution and seasonality
 761 of active fires as observed with the Terra and Aqua Moderate Resolution Imag-
 762 ing Spectroradiometer (MODIS) sensors. *Journal of Geophysical Research:
 763 Biogeosciences*, *111*, 2016. doi: 10.1029/2005JG000142
- 764 Giglio, L., Schroeder, W., & Justice, C. O. (2016). The collection 6 MODIS active
 765 fire detection algorithm and fire products. *Remote Sensing of Environment*,
 766 *178*, 31–41. doi: 10.1016/j.rse.2016.02.054
- 767 Groot, W. J. d., Field, R. D., Brady, M. A., Roswintiarti, O., & Mohamad, M.
 768 (2006, Sep 30). Development of the Indonesian and Malaysian fire danger rat-
 769 ing systems. *Mitigation and Adaptation Strategies for Global Change*, *12*(1),
 770 165. Retrieved from <https://doi.org/10.1007/s11027-006-9043-8> doi:
 771 10.1007/s11027-006-9043-8
- 772 Hao, N., Feng, Y., & Zhang, H. H. (2018). Model selection for high-dimensional
 773 quadratic regression via regularization. *Journal of the American Statistical As-
 774 sociation*, *113*(522), 615–625. doi: 10.1080/01621459.2016.1264956
- 775 Holloway, T., Levy, H., & Kasibhatla, P. (2000). Global distribution of carbon
 776 monoxide. *Journal of Geophysical Research: Atmospheres*, *105*(D10), 12123–
 777 12147. doi: 10.1029/1999JD901173
- 778 Islam, M. A., Chan, A., Ashfold, M. J., Ooi, C. G., & Azari, M. (2018, 9). Effects
 779 of el-niño, Indian Ocean dipole, and Madden-Julian oscillation on surface air
 780 temperature and rainfall anomalies over Southeast Asia in 2015. *Atmosphere
 781 2018, Vol. 9, Page 352, 9*, 352. Retrieved from [https://www.mdpi.com/
 782 2073-4433/9/9/352](https://www.mdpi.com/2073-4433/9/9/352) <https://www.mdpi.com/2073-4433/9/9/352> doi:
 783 10.3390/ATMOS9090352
- 784 Kalnay, E., Kanamitsu, M., Kistler, R., Collins, W., Deaven, D., Gandin, L.,
 785 ... Joseph, D. (1996). The NCEP/NCAR 40-year reanalysis project.
 786 *Bulletin of the American Meteorological Society*, *77*(3), 437 - 472. doi:
 787 10.1175/1520-0477(1996)077<0437:TNYRP>2.0.CO;2
- 788 Kistler, R., Kalnay, E., Collins, W., Saha, S., White, G., Woollen, J., ... Fiorino,
 789 M. (2001). The NCEP–NCAR 50-year reanalysis: Monthly means CD-ROM
 790 and documentation. *Bulletin of the American Meteorological Society*, *82*(2),
 791 247–268.
- 792 Madden, R. A., & Julian, P. R. (1972). Description of global-scale circula-
 793 tion cells in the tropics with a 40–50 day period. *Journal of Atmospheric
 794 Sciences*, *29*(6), 1109 - 1123. doi: 10.1175/1520-0469(1972)029<1109:
 795 DOGSCC>2.0.CO;2
- 796 Madden, R. A., & Julian, P. R. (1994). Observations of the 40–50-day tropical os-
 797 cillation—a review. *Monthly Weather Review*, *122*(5), 814 - 837. doi: 10.1175/
 798 1520-0493(1994)122<0814:OOTD(TO)>2.0.CO;2
- 799 Mason, S. A., Hamlington, P. E., Hamlington, B. D., Jolly, W. M., & Hoffman,
 800 C. M. (2017). Effects of climate oscillations on wildland fire potential in the

- 801 continental United States. *Geophysical Research Letters*, *44*, 7002-7010. doi:
802 10.1002/2017GL074111
- 803 N'Datchoh, E. T., Konaré, A., Diedhiou, A., Diawara, A., Quansah, E., & Assamoi,
804 P. (2015). Effects of climate variability on savannah fire regimes in West
805 Africa. *Earth System Dynamics*, *6*, 161-174. doi: 10.5194/ESD-6-161-2015
- 806 Neelin, J. D., Battisti, D. S., Hirst, A. C., Jin, F. F., Wakata, Y., Yamagata, T., &
807 Zebiak, S. E. (1998). ENSO theory. *Journal of Geophysical Research: Oceans*,
808 *103*(C7), 14261-14290. doi: 10.1029/97jc03424
- 809 Nelder, J. A. (1977). A reformulation of linear models. *Journal of the Royal Statisti-
810 cal Society. Series A (General)*, *140*(1), 48. doi: 10.2307/2344517
- 811 NOAA CPC. (2021). *Climate prediction center - teleconnections: Antarctic oscilla-
812 tion*. [https://www.cpc.ncep.noaa.gov/products/precip/CWlink/daily_ao
813 _index/ao/ao.shtml](https://www.cpc.ncep.noaa.gov/products/precip/CWlink/daily_ao_index/ao/ao.shtml).
- 814 NOAA OOPC. (2021). *Ocean observations panel for climate - state of the ocean cli-
815 mate*. <https://stateoftheocean.osmc.noaa.gov/>.
- 816 NOAA PSL. (2021). *Physical sciences laboratory - interpolated olr*. [https://psl
817 .noaa.gov/data/gridded/data.interp_OLR.html](https://psl.noaa.gov/data/gridded/data.interp_OLR.html).
- 818 Nur'utami, M. N., & Hidayat, R. (2016). Influences of IOD and ENSO to In-
819 donesian rainfall variability: Role of atmosphere-ocean interaction in the
820 Indo-pacific sector. *Procedia Environmental Sciences*, *33*, 196-203. doi:
821 10.1016/j.proenv.2016.03.070
- 822 Reid, J. S., Xian, P., Hyer, E. J., Flatau, M. K., Ramirez, E. M., Turk, F. J., ...
823 Maloney, E. D. (2012). Multi-scale meteorological conceptual analysis of ob-
824 served active fire hotspot activity and smoke optical depth in the Maritime
825 Continent. *Atmospheric Chemistry and Physics*, *12*(4), 2117-2147. doi:
826 10.5194/acp-12-2117-2012
- 827 Saji, N. H., Goswami, B. N., Vinayachandran, P. N., & Yamagata, T. (1999). A
828 dipole mode in the tropical Indian ocean. *Nature*, *401*(6751), 360-363. doi: 10
829 .1038/43854
- 830 Saji, N. H., & Yamagata, T. (2003). Possible impacts of Indian Ocean Dipole mode
831 events on global climate. *Climate Research*, *25*(2), 151-169. doi: 10.3354/
832 cr025151
- 833 Shabbar, A., Skinner, W., & Flannigan, M. D. (2011). Prediction of seasonal forest
834 fire severity in Canada from large-scale climate patterns. *Journal of Applied
835 Meteorology and Climatology*, *50*(4), 785-799. doi: 10.1175/2010JAMC2547.1
- 836 Shawki, D., Field, R. D., Tippet, M. K., Saharjo, B. H., Albar, I., Atmoko, D.,
837 & Voulgarakis, A. (2017). Long-lead prediction of the 2015 fire and haze
838 episode in Indonesia. *Geophysical Research Letters*, *44*(19), 9996. doi:
839 10.1002/2017GL073660
- 840 Thompson, D. W. J., & Wallace, J. M. (2000). Annular modes in the extratropi-
841 cal circulation. Part I: Month-to-month variability. *Journal of Climate*, *13*(5),
842 1000 - 1016. doi: 10.1175/1520-0442(2000)013<1000:AMITEC>2.0.CO;2
- 843 Tibshirani, R. (1996). Regression shrinkage and selection via the lasso. *Journal
844 of the Royal Statistical Society: Series B (Methodological)*, *58*, 267-288. doi: 10
845 .1111/J.2517-6161.1996.TB02080.X
- 846 Trenberth, K. (2013). *El Nino Southern Oscillation (ENSO)* (Tech. Rep.). National
847 Center for Atmospheric Research (NCAR).
- 848 van der Werf, G. R., Randerson, J. T., Giglio, L., Gobron, N., & Dolman, A. J.
849 (2008). Climate controls on the variability of fires in the tropics and subtrop-
850 ics. *Global Biogeochemical Cycles*, *22*(3). doi: 10.1029/2007GB003122
- 851 Voulgarakis, A., Marlier, M. E., Faluvegi, G., Shindell, D. T., Tsigaridis, K., &
852 Mängeon, S. (2015). Interannual variability of tropospheric trace gases and
853 aerosols: The role of biomass burning emissions. *Journal of Geophysical Re-
854 search: Atmospheres*, *120*(14), 7157-7173. doi: 10.1002/2014JD022926
- 855 Wheeler, M. C., & Hendon, H. H. (2004). An all-season real-time multivariate

- 856 MJO index: Development of an index for monitoring and prediction. *Monthly*
857 *Weather Review*, 132(8), 1917 - 1932. doi: 10.1175/1520-0493(2004)132<1917:
858 AARMMI>2.0.CO;2
- 859 Wooster, M. J., Perry, G. L., & Zoumas, A. (2012). Fire, drought and El Niño rela-
860 tionships on Borneo (Southeast Asia) in the pre-MODIS era (1980-2000). *Bio-*
861 *geosciences*, 9(1), 317–340. doi: 10.5194/bg-9-317-2012
- 862 Worden, H. M., Deeter, M. N., Edwards, D. P., Gille, J. C., Drummond, J. R., &
863 Nédélec, P. (2010). Observations of near-surface carbon monoxide from space
864 using mopitt multispectral retrievals. *Journal of Geophysical Research: Atmo-*
865 *spheres*, 115, 18314. doi: 10.1029/2010JD014242
- 866 Xavier, P., Rahmat, R., Cheong, W. K., & Wallace, E. (2014). Influence of
867 Madden-Julian Oscillation on Southeast Asia rainfall extremes: Observa-
868 tions and predictability. *Geophysical Research Letters*, 41(12), 4406–4412. doi:
869 10.1002/2014GL060241
- 870 Zhang, C.-H. (2010). Nearly unbiased variable selection under minimax concave
871 penalty. *The Annals of Statistics*, 38(2), 894–942. doi: 10.1214/09-AOS729